Soft Matter

Accepted Manuscript


Volume 1 | Number 1 | Jan 2013 | Pages 1–100

Soft Matter

www.rsc.org/softmatter

ROYAL SOCIETY OF CHEMISTRY

ROYAL SOCIETY OF CHEMISTRY

www.rsc.org/softmatter

Journal Name

ARTICLE TYPE

Cite this: DOI: 10.1039/xxxxxxxxxx

Deviation of sliding drops at a chemical step

Ciro Semprebon,[†a], Silvia Varagnolo[b], Daniele Filippi[b], Luca Perlini[b], Matteo Pierno[b], Martin Brinkmann[c], and Giampaolo Mistura[*b]

Received Date
Accepted Date

DOI: 10.1039/xxxxxxxxxx

www.rsc.org/journalname

The motion of partially wetting liquid drops in contact to a solid surface is strongly affected by contact angle hysteresis and interfacial pinning. However, the majority of models proposed for drops sliding over chemical surface patterns consistently neglect the difference between advancing and receding contact angles. In this article, we present a joint experimental and numerical study of the interaction of gravity driven drops with a chemical step formed at the junction between a hydrophilic and a hydrophobic region. It demonstrates the strong impact of a contact angle hysteresis contrast onto the motion of drops at a linear chemical step. Surprisingly, the smallest driving force required to drag the drop across the step onto the lower hydrophobic surface is not observed at a right angle of incidence. Our model reveals that the non–monotonous response of this passive drop 'filter' is solely due to the higher advancing contact angle on the lower surface, and creates an instance where drop motion is affected by dissipation at the contact line rather than by surface energy.

1 Introduction

The motion of fluid interfaces past solid substrates is crucial in many natural phenomena and technological processes, covering a wide variety of practical applications in daily life, industry, and agriculture[1–3]. Striking examples for passive control of interfacial flows are plants[4] and animals[5] that have adapted to a desert climate through their ability to retain and direct dew drops on part of their surfaces. Similar approaches to control small scale interfacial flows have been proposed in technological applications, including chemical patches[6–8], topographic structures[9,10], or embedded electrodes[11–13].

The majority of model studies[14–16] of wettability controlled drop motion considered highly idealized surfaces with negligible or vanishing wetting hysteresis. Most solids, however, display a pronounced 'static friction' of a three phase contact line caused by micro–scale heterogeneities that may trap the interface in metastable configurations. On the scale of the drop, these metastable shapes manifest in the form of interfacial pinning and history dependent contact angles.

In this article we present extensive experiments and numerical simulations to show that contact angle hysteresis is not simply a nuisance, but could be well exploited to direct and control the motion of wetting liquid drops. To demonstrate the profitable interplay of drop shape and liquid motion on surfaces with high contact angle hysteresis, we focus on gravity driven droplets[6,17,18] impinging on a straight boundary between two chemically different surfaces, as illustrated in Fig. 1a). At a finite tilt angle, the presence of the step breaks the reflection symmetry of the drop shape while the induced deformation creates a coupling of the drop mobilities into parallel and perpendicular directions. Such a 'cross–talk' would be hindered if the surfaces had a contrast in surface energy but vanishing contact angle hysteresis. The rich spectrum of dynamic regimes caused by the mobility coupling in the presence of a contact angle hysteresis contrast are quantified in systematic numerical simulations based on a contact line friction model[19]. Renderings of typical drop shapes at the step are shown in Fig. 1 b).

2 Experimental

Sliding measurements were performed through the experimental setup depicted in Fig. 1a). We used drops of a 80% w/w glycerol/water solution with density $\rho = 1.21$ g/cm^3, viscosity $\eta = 52$ cP, i.e. fifty times more viscous than pure water, and with a surface tension $\gamma = 65.3$ mN/m at T=23°C. The substrate was a polycarbonate (PC) slab having a thickness of 5 mm and a side length of 5 cm. To realize the chemical step, half of the original protective cover was kept as a mask for the deposition of a molecular layer of trichloro(1H, 1H, 2H, 2H-perfluorooctyl)silane (TFOS) from the vapor phase. The removal of the cover produced two chemically distinct areas separated by a linear bound-

---

[a] Department of Mechanical Engineering, University of Edinburgh, Edinburgh EH9 3FB, UK

[b] Dipartimento di Fisica e Astronomia 'G.Galilei' - DFA, Università di Padova, via Marzolo 8, 35131 Padova, Italy

[c] Experimental Physics, Saarland University, 66123 Saarbrücken, Germany

[†] E-mail: ciro.semprebon@ed.ac.uk

[*] E-mail: giampaolo.mistura@unipd.it

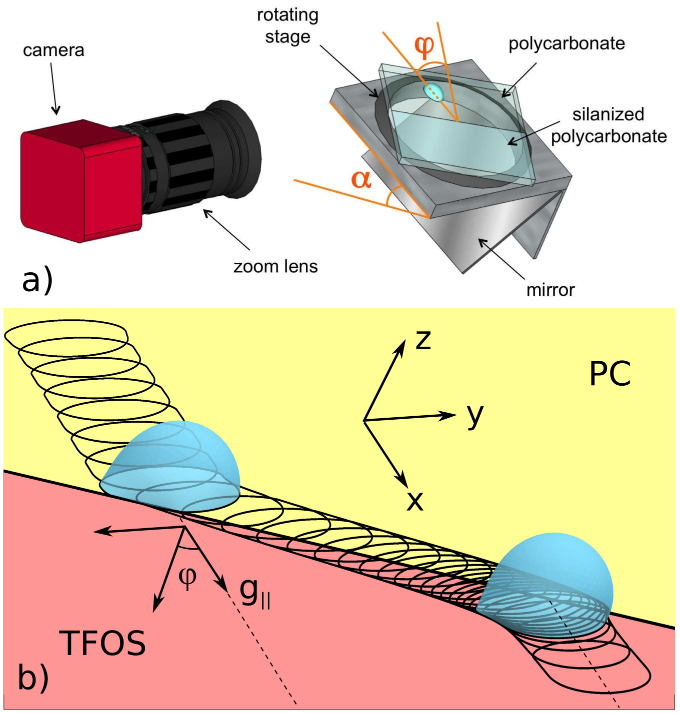

Fig. 1 a) Sketch of the experimental setup indicating the inclination angle α with the respect to gravity and the tilt angle φ with the respect to the direction of the in-plane body force. b) Rendering of the simulations for $\varphi = 50^\circ$ and Bo $= 1.35$. PC (TFOS) indicates the polycarbonate (silanized) region of the wettability step. The coordinate system x, y, z in the tilted frame employed in the simulations is indicated.

ary. The advancing and receding contact angles on the PC region, where the drops were initially deposited, were respectively $\theta_{\mathrm{a,PC}} = 88^\circ \pm 2^\circ$ and $\theta_{\mathrm{r,PC}} = 63^\circ \pm 3^\circ$, while those on the TFOS covered portion, beyond the chemical step, were $\theta_{\mathrm{a,TFOS}} = 118^\circ \pm 2^\circ$ and $\theta_{\mathrm{r,TFOS}} = 64^\circ \pm 4^\circ$.

Drops of volume $V = (40 \pm 2)$ μl were deposited on the already inclined plane by means of a vertically mounted syringe pump. The sample was placed on a manually rotating stage with a central opening that could change the inclination φ of the linear chemical step. The stage was mounted on a rotating tilting support whose inclination angle α could be set by a computer with 0.1° accuracy[7]. The drop was lightened by two white LED back-lights. The lateral profile of the drop was viewed with a CMOS camera mounted along the rotation axis of the plate and equipped with a macro zoom lens. By moving the camera, it was possible to focus on the image of the drop contact line reflected by a mirror mounted under the sample holder at 45° with respect to the substrate. Acquired images, where drops appear dark on a light background, were analysed through a custom–made LabVIEW script[20].

Varying α between 25° and 60°, the in–plane component of the body force can be described by a Bond number Bo $= \rho g V^{2/3} \sin\alpha/\gamma$ (where g is the gravity acceleration) ranged between 0.9 and 1.8. The typical velocities of the drop steadily sliding on the PC region before touching the step ranged between $U \sim 0.1$ mm/s and $U \sim 10$ mm/s. Accordingly, the maximum Weber and Capillary number of the drop with dimension $L_0 \sim V^{1/3}$ were We $= \rho U^2 L_0/\gamma \sim 3 \cdot 10^{-3}$ and Ca $= \eta U/\gamma \sim 0.01$, respectively, indicating that drop motion was governed by an interplay of gravity and interfacial forces. Capillary waves on the drop interface that may be excited during collision with the chemical step are quickly damped away as the Ohnesorge number Oh $=$ Ca/We$^{1/2} \sim 0.15$ is close to unity. In addition, when crossing the chemical step, the contact line velocity is further reduced to the order of $U \sim 0.01$ mm/s. In this velocity regime, and for many experimental systems, the dissipation of the moving contact line conforms better to the predictions of the molecular kinetic approach[21] rather than to the dependence expected for viscous flows in the fluid wedge region[22]. Hence, we model the drop shapes in our simulations as quasi–static while the drop motion was solely governed by contact line mobility.

3 Contact line friction model

The essential physics of the present experimental system is captured by a minimal model based on a local contact line mobility. This model naturally combines static contact angle hysteresis and dynamic contact angles[19,23], and is ideally suited to describe the motion of slowly sliding drops close to the pinning and depinning thresholds.

In this 'contact line friction model', the shape of the liquid interface is assumed to be in mechanical equilibrium, and therefore at each instant fulfils the Laplace law

$$\Delta P + \rho\, g_{\parallel}\, x \; = 2\gamma\kappa \tag{1}$$

where ΔP is the pressure jump across the liquid interface at $x = 0$, γ the liquid–vapour tension, κ the local mean curvature, and $g_{\parallel} = g \sin\alpha$ the in–plane component of the acceleration of gravity acting in the downhill x–direction, cf. also Fig. 1. Observing that for our experimental parameters the deformation of the drop due to the component $g_{\perp} = g\cos\alpha$ normal to the substrate has a minimal impact on the location of the boundaries between different mechanisms occurring at the chemical step, we omitted it in the rest of our calculations. In the limit of negligible deformations the Bond number Bo $= \rho g V^{2/3}/\gamma$ and the inclination angle φ represent the minimal set of control parameters for the system.

For a given contour Γ of the contact line, being not necessarily in mechanical equilibrium, the shape Σ of the free liquid interface is described by a minimum of the energy functional

$$\mathscr{E}\{\Sigma\} = \gamma A_{\mathrm{lv}} - \rho\, g_{\parallel}\, V \,\langle x \rangle \tag{2}$$

where A_{lv} is the area of the free interface, while $\langle x \rangle$ denotes the x-coordinate of the drops' center of mass. As we were operating exclusively in the limit of small contact line velocities, we employed a linear relation between contact line velocity and dynamic contact angles

$$u = \begin{cases} u_{\mathrm{a}}(\theta - \theta_{\mathrm{a}}) & \text{for} \quad \theta \geq \theta_{\mathrm{a}} \\ u_{\mathrm{r}}(\theta - \theta_{\mathrm{r}}) & \text{for} \quad \theta \leq \theta_{\mathrm{r}} \end{cases} , \tag{3}$$

where u_a and u_r were assumed to be constant over a homogeneous portion of substrate.

The numerical implementation follows the method introduced

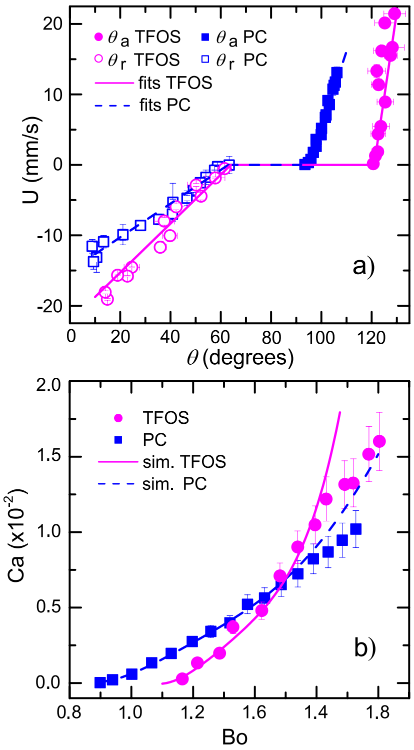

Fig. 2 a) Experimental measurements of the dynamic advancing and receding angles for PC and TFOS substrates, with linear fits providing the phenomenological parameters for the simulation. Positive (negative) velocities refer to advancing (receding) motion. b) Relation between Bo and Ca for drops in steady motion on PC and TFOS. Lines are the numerical results.

in our previous work[19] where the drop shape Σ is subject to the global constraint of a fixed liquid volume V. We employed the free software Surface Evolver[24] to represent the free interface by a triangulated mesh and minimize the energy Eq. (2) with standard minimization algorithms. The mesh is gradually refined close to the contact line such as the contact line typically comprises ~ 300 elements. The algorithm to simulate the temporal evolution of the droplet shape contains two steps: in the first step the energy of the drop is minimised given the contour Γ_n of the contact line at time t_n. In the second step, after convergence of the interfacial shape, the local contact angle θ at each edge of Γ_n is evaluated. If $\theta_r \le \theta \le \theta_a$ is satisfied for both the edges connected to a node of Γ_n, the contact line around the node is in a pinned state and will not be moved. Whenever the local contact angle of at least one of the neighbouring edges is found outside the hysteresis interval, i.e., $\theta > \theta_a$ or $\theta < \theta_r$, the node is moved. To perform the motion of the contact line between time t_n and $t_{n+1} \equiv t_n + \Delta t$, a virtual displacement $\Delta \mathbf{r} = \mathbf{n} u \Delta t$ is first assigned to each edge of Γ_n, where $\mathbf{n}$ is the co-normal vector of the contact line in the plane of the substrate. The new contact line contour G_{n+1} is then obtained by moving each node according to a weighted average of the virtual displacements assigned to the neighbouring edges. At this point, an updated interfacial shape for a new contact line contour has to be computed with a standard minimisation algorithm. The drop shape is evolved in time by a cyclic repetition of the two steps. To reduce the computational time we use an adaptive time step chosen such that the maximum displacement is 10% of the length of the shortest element of the contact line. During time evolution, contact line elements are constantly generated and removed in order to maintain a constant quality of the mesh. In particular, elements are generated at the leading edge and are constantly shifted to the drop side during the evolution. Eventually, they are destroyed when collected by the trailing edge.

To match simulations with the experiments, the phenomenological parameters u_a and u_r were obtained by fitting the relation between contact line velocity and dynamic contact angles derived from the experiments on PC and TFOS substrates in Fig. 2a): $u_{a,PC} = 61.6$ mm s^{-1}rad^{-1}, $u_{r,PC} = 13.7$ mm s^{-1}rad^{-1}, $u_{a,TFOS} = 138$ mm s^{-1}rad^{-1}, $u_{r,TFOS} = 19.9$ mm s^{-1}rad^{-1}. Figure 2b) reports a direct comparison of the relation between dimensionless drop velocity Ca and driving force Bo with the experimental data of steady drops sliding on homogeneous PC and TFOS surfaces. Very good agreement was found on both substrates for Bo < 1.6 while numerical data overestimate the experimental results at larger Bond numbers.

A possible cause for the discrepancy at high Bond numbers is the transition to a regime where the viscous dissipation in the bulk cannot be any more neglected. The assumption that the dissipation is mostly localized at the moving contact line is not valid for interfaces in contact to substrates with small contact angles and low contact angle hysteresis. In this case, viscous dissipation in the liquid wedge close to the three–phase contact line, and to a smaller extent also in the bulk, dominate drop motion[25], and demand solutions of the full–scale fluid dynamic problem[6].

Simulations of drops approaching the chemical step are initialised with a drop at rest in the PC portion of the surface. The body force is subsequently applied at the prescribed angle with respect to the chemical step. As we showed in a previous work[19], for sufficiently low Bo, and for certain initial conditions, the drop can remain in a pinned state even tough a steady sliding solution exists. For the range of Bo explored in our experiment this case does not occur. In our case, experiments and numerical simulations can be safely compared because the drop reaches a steady sliding before hitting the chemical step and a sliding drop looses all the information inherent to its initial configuration.

4 Results and Discussion

We observed four distinct scenarios for the drop approaching the chemical step as summarized in Fig. 3: a) at low Bo and φ the drop is simply pinned at the step; b) at high Bo and intermediate φ the drop crosses the step; c) at high φ the drop glides along the step without crossing it; d) at intermediate Bo and φ the drop glides for a short distance (at least 2 mm) along the step until arrest, and remains pinned. By systematically varying the angles α and φ, we constructed the dynamical phase diagram plotted in the graph of Fig. 3e). Filled symbols of different colors and shapes represent the path followed by the drop approaching the chemical step. No data are reported for Bo ≤ 1 because drops slide very slowly and it was very difficult to distinguish the different crossing cases. The regions identifying the four regimes are delimited by connected open symbols obtained from the analysis of systematic numerical simulations. They show a good agree-

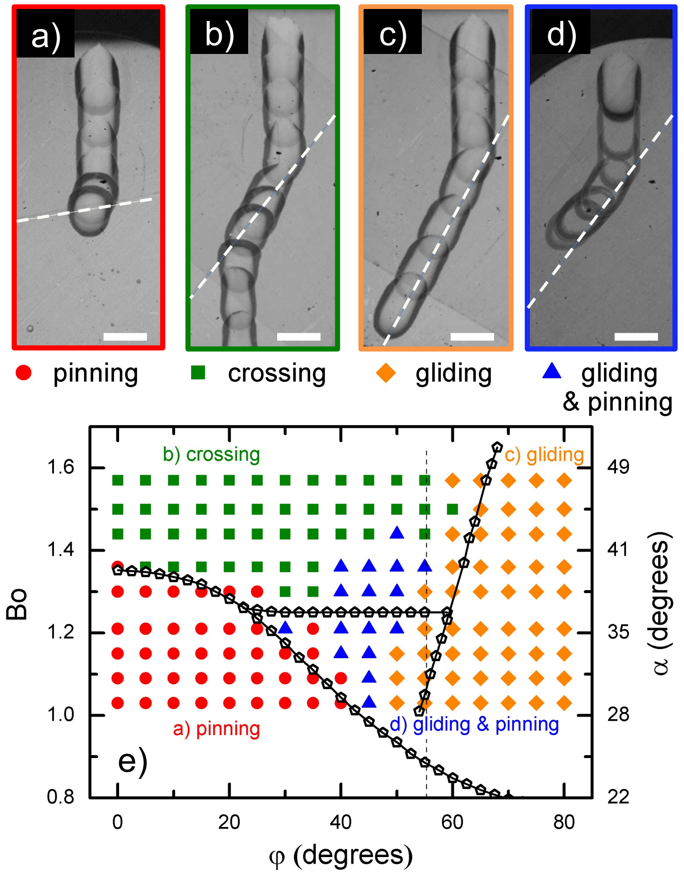

Fig. 3 Sequence of the four possible drop trajectories exhibited by a drop approaching the chemical step: a) the drop pins; b) the drop crosses the step; c) the drop slides along the step; d) the drop partially slides along the step and pins in a later stage. The dashed inclined lines mark the chemical step and the horizontal scale bars correspond to 5 mm. e) Dynamical phase diagram showing the four regions in the φ–Bo space. Filled symbols refer to experiments, while open symbols are evinced from simulations. Connecting lines are guide for the eye. See text for further details.

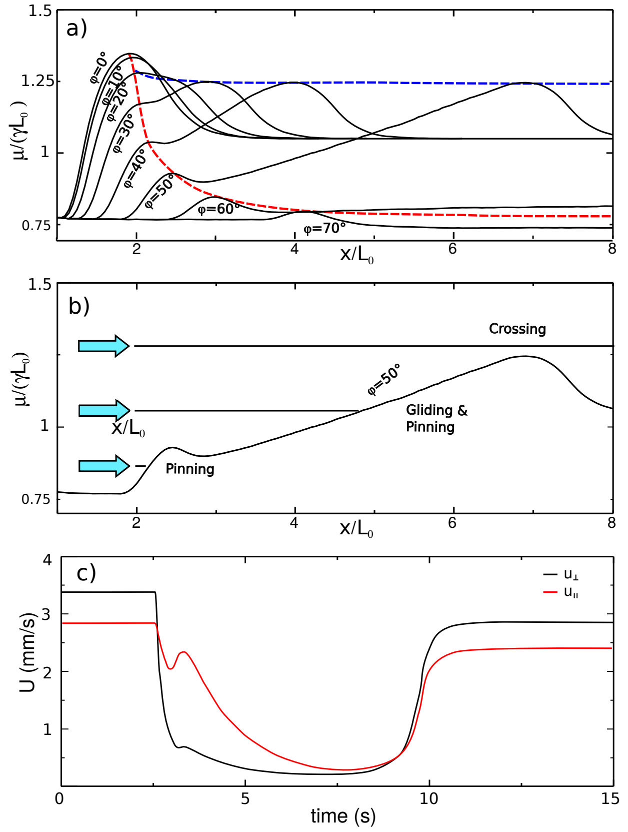

Fig. 4 a) Force evolution during crossing for various values of φ. The dashed lines indicate the trend of the two peaks present in the curves. b) Construction of three crossing scenarios for the case $\varphi = 50^\circ$. c) Parallel and perpendicular velocity components of the drop centre of mass when crossing the step for $\varphi = 50^\circ$ and $\mathrm{Bo} = 1.35$. Series of force curves as a function of the position x of the center of mass, normalized by $L_0 = V^{1/3}$, for φ varied in steps of 10°. Here the drop is initially placed at $x = 0$, while the position of the chemical step shifted forward with increasing φ for better visibility.

ment with the experimental results, considering the unavoidable presence of various sources of defects and noise in the system. In particular, the transition curve separating the pinning region from the gliding and pinning one occurs at somewhat smaller φ values. This could be due to the presence of substrate defects that enhance the pinning of the drop. Furthermore, the transition with the gliding region occurs at larger φ values, suggesting that most of the microscopic defects are located on the TFOS side.

The results present two counter–intuitive aspects. First, one would expect the minimum Bond number $\mathrm{Bo}_{\mathrm{min}}$ necessary to let the drop cross the step to grow with φ, because the component of the body force perpendicular to the step decreases as $\cos\varphi$. Instead we observed an initial decrease of $\mathrm{Bo}_{\mathrm{min}}$ for $\varphi < 25^\circ$, as φ increased. In other words, the optimal direction for crossing is not perpendicular to the step. To prove that such unexpected result is determined by the contact angle hysteresis, we performed simulations by taking two different equilibrium angles $\theta = \theta_a = \theta_r$ at the two sides of the step, with the drop crossing from the more hydrophilic to the more hydrophobic. Regardless of the chosen combination of angles, we always observed a monotonous increase of body force proportional to $1/\cos\varphi$, as suggested by a simple decomposition of the body force along the direction perpendicular and parallel to the straight boundary. In this case the dynamical phase diagram is less complex, showing only the crossing and gliding regimes. The second counter–intuitive aspect is the re–entrant shape of the boundary to the gliding region in the range $50^\circ \lesssim \varphi \lesssim 60^\circ$: for φ around 55° (see dashed line in Fig. 3e)), rising Bo from low to high values we first found the transition between pinning and gliding. Upon increasing Bo we noticed a transition between gliding and gliding followed by pinning. Only at higher values of Bo we observed drops crossing the step. This means that the increase of the body force can induce pinning of a drop otherwise in motion.

To further gain insight into the mechanism that hinders or allows crossing of the drop, we computed the associated force evolution. To this end we dropped the potential energy term in Eq. (2) and applied instead an additional global constraint on the downhill center of mass position, $\langle x \rangle$. The y–component of the center of mass was then allowed to freely adapt to the value that minimizes the total energy. To compute the force evolution, we quasi–statically shifted the position of the center of mass along the direction of the body force. In this case, the retaining force in our simulations is given by the Lagrange multiplier μ related to the constraint of a fixed $\langle x \rangle$. At each increment, we allowed the contact line to relax until all the contact angles lied within the static hysteresis interval. As shown in the series of force evolutions Fig. 4 a), when the drop collides with the step, μ rises because of the contact line deformation. For small φ, the curves exhibit a single peak, while at larger φ the curves show a second one. Here the new rise of the force is related to the progressive shift of the drop from the low hysteresis PC to the high hysteresis TFOS region. Similarly to what observed for the case of depinning from an initially circular contact line[19], the second peak occurs when the drop escapes from the self–created constriction of the contact line. With increasing φ, the magnitude of both peaks decreases. While the first peak vanishes in the limit $\varphi \to 90^\circ$, the second peak approaches a constant value. Furthermore the distance of the second peak from the contact point asymptotically diverges when φ increases, and completely disappears from our simulation domain for $\varphi > 50^\circ$.

The analysis of the landscape allows to identify all four experimentally observed dynamical regimes for a drop approaching the tilted chemical step. In Fig. 4b) the body force is represented by blue arrows on the left side. If Bo is lower than the first peak, the drop simply pins after touching the step. If the value of Bo falls into the interval between the two peaks, the drop glides along the step and pins afterwards. The extension of gliding before pinning and the deviation of the drop trajectory is controlled by the rate of rise of the second peak. Only if Bo exceeds the height of the second peak, the drop will cross the step. The sequences of peaks as a function of φ accurately match the transition lines in Fig. 3 between crossing and pinning, and between crossing and gliding with pinning. The absence of the second peak at larger φ implies that the drop is entirely repelled by the step, corresponding to the gliding observed in the experiments. The boundary of the gliding region cannot be determined from the analysis of the force landscape. The line displayed in Fig. 3 is obtained by mapping the results of several sequences of simulations, and can be approximately described by $\mathrm{Bo} \simeq \mathrm{Bo}_\perp / \cos\varphi$. Here $\mathrm{Bo}_\perp \simeq L(\cos\theta_{\mathrm{r,PC}} - \cos\theta_{\mathrm{a,TFOS}})$, L being the projection of the drop elongation perpendicular to the step. Such relation implies that the drop mobility can be split in two independent components. While without contact angle hysteresis this is valid for the full range of φ, with hysteresis the decomposition is valid only for large φ, and in both cases it corresponds to the transition to gliding. Figure 4 c), reports the two components of the velocity profile corresponding to the trajectory shown in Fig. 1 b). For drops coming from the upper (PC) substrate, the first touch of the chemical step causes a fast decrease of the drop velocity. After a local minimum, the velocity slightly increases in the parallel component, due to squeezing and alignment of the drop along the step. Consequently the drop starts a slow side–ward shift to the lower (TFOS) substrate, which causes a further decrease of the velocity. Eventually the drop escapes from the chemical step and the retaining force decreases, causing a quick acceleration, until reaching a steady motion on the TFOS substrate.

5 Discussion and conclusions

In this work we measured the drop deflection of sliding drops in the regime of small Weber and Capillary numbers induced by a chemical step placed at an arbitrary orientation with respect to the direction of the in plane body force. Our experimental results show that the magnitudes of both advancing and the receding contact angle govern the motion of sliding drops on chemical heterogeneous surfaces. The rich phenomenology of dynamic regimes arises from a cross–talk between drop deformations and the mobility parallel and perpendicular to the discontinuity. Both Capillary number Ca and Weber number We account for the droplet velocity. For a Ohnesorge number $Oh = \mathrm{Ca}/\mathrm{We}^{1/2} \lesssim O(1)$, inertial effects will become visible if $\mathrm{We} \gtrsim O(1)$[12]. Conversely, if $\mathrm{Oh} \gtrsim O(1)$ the shape will be influenced more by viscous stresses once $\mathrm{Ca} \gtrsim O(1)$. We expect that the droplets tend to deform into the direction of motion for the case $\mathrm{Oh} \gtrsim O(1)$ for increasing Ca, and eventually show a transition to pointed tip and pearling instability at the rear[25]. Furthermore we expect that the dominant effect of inertia will be shape oscillations when the drop hits the step. For a step perpendicular to the direction of motion[12], the energy stored into the shape oscillations can reduce the pinning effect. While a similar effect can be expected also for highly hysteretic substrates, to predict the influence of inertia on the shape of sliding drops hitting a step having arbitrary direction it is necessary to consider the oscillation modes induced by the symmetry breaking.

In this work we considered the case of two close receding contact angles and an increased advancing CA on the lower surface found in our experimental system. In principle, all four contact angles can be varied independently, and preliminary investigations suggest the presence of qualitatively different crossing diagrams. We plan to address in more detail the full range of contact angles involved in this problem in a forthcoming work. This study underlines that contact angle hysteresis is a key to describe, and to further predict the motion of drops on complex wettability patterns in the limit of small interfacial velocities. The present model could be of help to design devices for passive drop manipulation, with potential applications in fog–harvesting, controlled liquid condensation, or drop sorting.

C.S. thankfully acknowledges Halim Kusumaatmaja and Timm Krüger for inspiring discussions. M.B. and G.M. gratefully acknowledge the Vigoni exchange program between the Ateneo Italo-Tedesco and the German Academic Exchange Service (DAAD). We are particularly grateful to Paolo Sartori for kind support in the set-up preparation.

References

1 D. Bonn, J. Eggers, J. Indekeu and J. Meunier, *Rev. Mod. Phys.*, 2009, **81**, 739–805.
2 D. Quéré, *Annu. Rev. Mater. Res.*, 2008, **38**, 71–99.
3 K. Liu, X. Yao and L. Jiang, *Chem. Soc. Rev.*, 2010, **39**, 3240–3255.
4 J. Ju, H. Bai, Y. Zheng, T. Zhao, R. Fang and L. Jiang, *Nature Communications*, 2012, **3**, 1247.
5 A. R. Parker and C. R. Lawrence, *Nature*, 2001, **414**, 33–34.

6 S. Varagnolo, D. Ferraro, P. Fantinel, M. Pierno, G. Mistura, G. Amati, L. Biferale and M. Sbragaglia, *Phys. Rev. Lett.*, 2013, **111**, 066101.

7 S. Varagnolo, V. Schiocchet, D. Ferraro, M. Pierno, G. Mistura, M. Sbragaglia, A. Gupta and G. Amati, *Langmuir*, 2014, **30**, 2401–2409.

8 A. Nakajima, Y. Nakagawa, T. Furuta, M. Sakai, T. Isobe and S. Matsushita, *Langmuir*, 2013, **29**, 9269–9275.

9 Y. V. Kalinin, V. Berejnov and R. E. Thorne, *Langmuir*, 2009, **25**, 5391–5397.

10 J. C. Baret, M. M. J. Decré, S. Herminghaus and R. Seemann, *Langmuir*, 2007, **23**, 5200–5204.

11 D. J. C. M. ’t Mannetje, C. U. Murade, D. van den Ende and F. Mugele, *Appl. Phys. Lett.*, 2011, **98**, 014102.

12 D. J. C. M. ’t Mannetje, S. Ghosh, R. Lagraauw, S. Otten, A. Pit, C. Berendsen, J. Zeegers, D. van den Ende and F. Mugele, *Nat. Commun.*, 2014, **5**, 3559.

13 P. Brunet, M. Baudoin, O. B. Matar and F. Zoueshtiagh, *Physical review. E, Statistical, nonlinear, and soft matter physics*, 2010, **81**, 036315.

14 H. Kusumaatmaja and J. M. Yeomans, *Langmuir*, 2007, **23**, 956–959.

15 M. Sbragaglia, L. Biferale, G. Amati, S. Varagnolo, D. Ferraro, G. Mistura and M. Pierno, *Phys. Rev. E*, 2014, **89**, 1–12.

16 A. Cavalli, M. Musterd and F. Mugele, *Phys. Rev. E*, 2015, **91**, 1–10.

17 M. A. Nilsson and J. P. Rothstein, *Phys. Fluids*, 2012, **24**, 062001.

18 S. Suzuki, A. Nakajima, K. Tanaka, M. Sakai, A. Hashimoto, N. Yoshida, Y. Kameshima and K. Okada, *Appl. Surf. Science*, 2008, **254**, 1797–1805.

19 C. Semprebon and M. Brinkmann, *Soft Matter*, 2014, **10**, 3325.

20 T. Toth, D. Ferraro, E. Chiarello, M. Pierno, G. Mistura, G. Bissacco and C. Semprebon, *Langmuir*, 2011, **27**, 4742–4748.

21 T. D. Blake, a. Clarke, J. DeConinck and M. J. DeRuijter, *Langmuir*, 1997, **13**, 2164–2166.

22 R. Fetzer and J. Ralston, *J. Phys. Chem. C*, 2010, **114**, 12675–12680.

23 M. Musterd, V. van Steijn, C. R. Kleijn and M. T. Kreutzer, *Phys. Rev. Lett.*, 2014, **113**, 066104.

24 K. A. Brakke, *Philos. T. Roy. Soc. A*, 1996, **354**, 2143–2157.

25 N. Le Grand, A. Daerr and L. Limat, *J. Fluid Mech.*, 2005, **541**, 293.

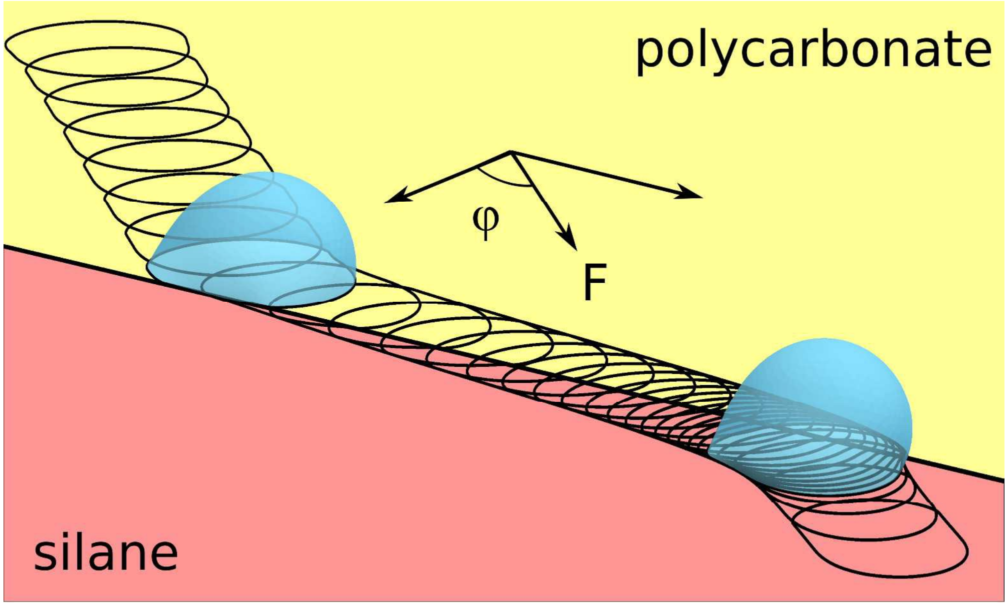

1058x635mm (72 x 72 DPI)